International Journal of Multiphase Flow 37 (2011) 46–54

Contents lists available at ScienceDirect

International Journal of Multiphase Flow

journal homepage: www.elsevier.com/locate/ijmulflow

# An inhomogeneous three-phase model for the flow in aluminium reduction cells

Jie Li, Yujie Xu *, Hongliang Zhang, Yanqing Lai

*School of Metallurgical Science and Engineering, Central South University, Changsha 410083, PR China*

ARTICLE INFO

*Article history:*
Received 13 October 2009
Received in revised form 27 August 2010
Accepted 27 August 2010
Available online 18 September 2010

*Keywords:*
Aluminium reduction cell
Inhomogeneous three-phase flow
Current efficiency model

ABSTRACT

The exact prediction of both the melts flow and metal–bath interface deformation is critical to the design of commercial aluminium reduction cells which operate steadily at high current efficiency (CE). An inhomogeneous flow model of three phases, metal, bath and gas bubbles, was established in this study. The flow in a 300 kA cell was numerically computed with the model by using the finite volume scheme, and the results reveal the relation among the motion of the three phases and prove that the globality of the flow in cells could not be neglected. An improved calculation model of CE, based on the surface renewal theory, was also developed by connecting the melts flow with the mass transfer of reduced entity at the metal–bath interface. Using the model, the local CE in the 300 kA cell was predicted, and the calculated CE value of the whole cell is reasonable.



## 1. Introduction

Aluminium is manufactured by reducing alumina in a Hall–Héroult cell, in which a layer of electrolyte (bath) floats a pool of molten aluminium (metal) and gas bubbles, generated on anode surfaces, induce the liquid motion in the process of floating upward to escape. In addition, the intense current, passing the cell and bus bars, and associated magnetic field cause electromagnetic forces (EMFs), which act on the whole fluid region. Therefore, regardless of the minor influence of alumina solid particles, the system under research is a three-phase flow, driven by EMFs, with one dispersed gaseous phase and two continuous liquid phases that can be treated as Newtonian viscous incompressible fluids (Ai, 1985). A transverse cross-sectional schematic of a modern aluminium reduction cell is shown in Fig. 1.

Previous studies either neglected the gas bubble phase (Severo et al., 2005) or adopted the method of flow partition first proposed by Ai (1985). For the latter, as the fluid region in a cell is artificially divided into two or three layers according to the fluid characteristic, the metal flow and the bubble-included bath flow were usually computed and studied separately, which transform the subject into the models of single-phase or two-phase flow (Robl, 1983; Wu et al., 2003; Zhou et al., 2003; Doheim et al., 2007). However, the metal flow and the bath flow are affected by both the momentum transfer between the two continuous phases in horizontal direction, through a shear layer at the interface, and that in vertical direction, enhanced by the considerable vertical EMFs that derive from horizontal current in a cell. Moreover, the interphase force between the two phases plays a significant role in the deformation of the metal–bath interface, which determines the distribution of anode–cathode distance (ACD), one of the most important parameters in aluminium electrolysis. A model of inhomogeneous three-phase flow can introduce the interrelations among the motion of the three phases, and compute the volume fraction of each phase so as to obtain the metal–bath interface, which was estimated in the model of one or two-phase flow, using an approximate method on the basis of the principle that pressure in fluid is continuous (Blanc and Entner, 1980; Wu et al., 2003; Zhou et al., 2003). On the other hand, a model covering the whole fluid region needs to study, since a local one may fail to characterize the overall flow in a cell due to the asymmetry of electric and magnetic fields. In one word, the whole three-phase flow model, presented in this paper, coincides with the real fluid system in cells and adequately takes account of the globality of the melts motion.

The current efficiency (CE), referred to the production of aluminium, is considered one of the key technical targets described the performance of the cells, and CE decreases caused by the mass transfer of metal in some electrochemical process, which has certain relation with the melts motion in cells. Sterten (1988) studied the mechanism of current loss and developed a CE model not involving the effect of the melts flow. Assuming the metal–bath interface was a solid wall, a simplified model connecting current loss with the mass transfer coefficient of the reduced entity, calculated with some results from the bath flow simulation, was reported by Haarberg et al. (1998), while, in this paper, an improved model of CE based on the surface renewal theory is presented.

* Corresponding author.
*E-mail address:* sqjsxu@gmail.com (Y. Xu).

0301-9322/$ - see front matter © 2010 Elsevier Ltd. All rights reserved.
doi:10.1016/j.ijmultiphaseflow.2010.08.009

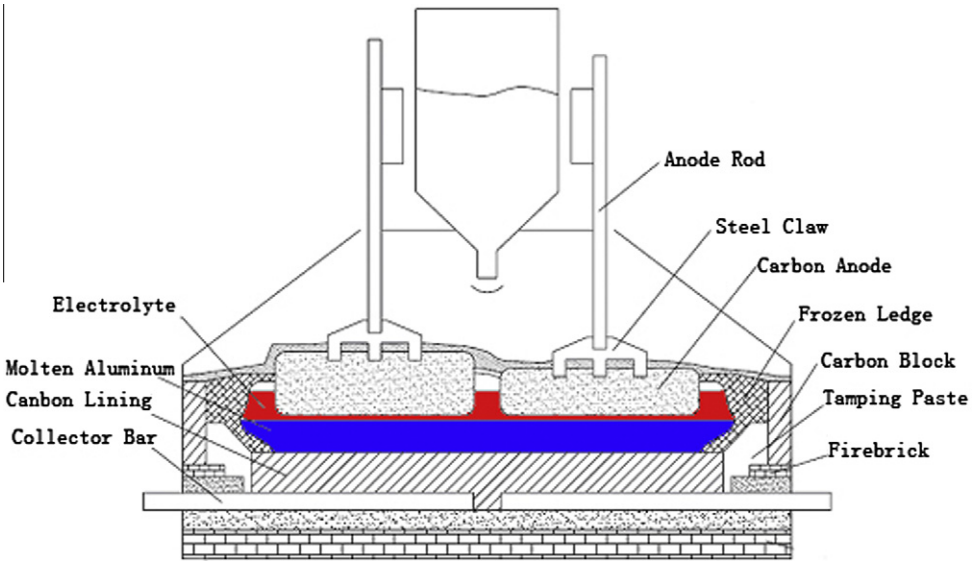


**Fig. 1.** Cross section of a modern aluminium reduction cell.

## 2. Computational model

### 2.1. The governing equation

In our study, the three-phase flow in aluminium reduction cells was computed based on the Euler/Euler approach by solving the time-averaged Navier–Stokes equations which was widely used in large-scale engineering problems for its practicability. In this case, an inhomogeneous equation for conservation of mass can be written as:

$$\frac{\partial}{\partial t}(r_\alpha \rho_\alpha) + \nabla \cdot (r_\alpha \rho_\alpha U_\alpha) = 0 \tag{1}$$

where $U_\alpha$, $r_\alpha$, and $\rho_\alpha$ are velocity, volume fraction and density of phase $\alpha$, respectively. The corresponding equation for conservation of momentum is given as:

$$\begin{aligned} &\tfrac{\partial}{\partial t}(r_\alpha \rho_\alpha U_\alpha) + \nabla \cdot (r_\alpha(\rho_\alpha U_\alpha \times U_\alpha)) \\ &= -r_\alpha \nabla p_\alpha + \nabla \cdot (r_\alpha \mu_{\alpha eff}(\nabla U_\alpha + (\nabla U_\alpha)^T)) + S_{M\alpha} + M_\alpha \end{aligned} \tag{2}$$

where $\mu_{\alpha eff}$ is effective viscosity of phase $\alpha$, a sum of molecular viscosity $\mu_\alpha$ and eddy viscosity $\mu_T$, $M_\alpha$ describes the interfacial forces acting on phase $\alpha$ due to the presence of other phases (interphase drag force was only considered in this article), and $S_{M\alpha}$ describes the momentum sources due to external body forces, which mainly include EMFs and buoyancy for this study. In addition, the volume fraction sum to unity:

$$\sum_{\alpha=1}^{3} r_\alpha = 1 \tag{3}$$

For the bath and metal, the two liquid phases, the terms ($\mu_{\alpha eff}$, $M_\alpha$ and $S_{M\alpha}$) in Eq. (2) is different and given as Table 1, where $F_{EM}$ is volume density of EMFs and $C_{\partial,\beta}$ is a coefficient for describing drag force between phase $\alpha$ and phase $\beta$. In this article, the subscript '$b$', '$m$' and '$p$' denote bath, metal and gas bubble (particles), respectively.

**Table 1**
Variables of the momentum conservation equation.

| $\alpha$ | $\mu_{\alpha eff}$ | $S_{M\alpha}$ | $M_\alpha$ |
|---|---|---|---|
| Bath | $\mu_b + \mu_T$ | $r_b F_{EM}$ | $C_{b,m}(U_m - U_b) + C_{b,p}(U_p - U_b)$ |
| Metal | $\mu_m + \mu_T$ | $r_m(\rho_m - \rho_b)g + r_m F_{EM}$ | $C_{m,b}(U_b - U_m)$ |

### 2.2. Calculation of the interphase drag force

#### 2.2.1. The drag force between the melts and bubbles

Assuming that the bubble phase is present as particles with equivalent diameter $d_p$, the coefficient $C_{b,p}$ depends on the drag coefficient ($C^D_{b,p}$) and the interfacial area density ($A_{b,p}$) between phase $\alpha$ and bubbles, as follow:

$$C_{b,p} = \frac{C^D_{b,p}}{8} A_{b,p} \rho_b |U_p - U_b| \tag{4}$$

with

$$A_{b,p} = \frac{6 r_p}{d_p} \tag{5}$$

The bubbles are moving under the influence of gravity, surface tension, and friction exerted by the liquid on their surface. To measure the ratio between gravitational and surface tension forces, the dimensionless Eötvös number ($Eo$) was used:

$$Eo = \frac{\Delta \rho g \cdot d_p^2}{\sigma_{st}} \tag{6}$$

Here $\Delta\rho$ is the density difference between the phases, $g$ is the gravitational acceleration, and $\sigma_{st}$ is the surface tension coefficient.

Then the drag coefficient ($C^D_{b,p}$) between the liquid and the bubbles was calculated, referring to the correlations proposed by Ishii and Zuber (1979), as follows:

$$\begin{aligned} C^{D,sph}_{b,p} &= \max\left(\tfrac{24}{\mathrm{Re}_p}\left(1 + 0.1\mathrm{Re}_p^{0.75}\right), 0.44\right) \\ C^{D,dist}_{b,p} &= \min\left(\tfrac{2}{3} Eo^{1/2}, \tfrac{8}{3}\right) \\ C^{D}_{b,p} &= \max\left(C^{D,sph}_{b,p}, C^{D,dist}_{b,p}\right) \end{aligned} \tag{7}$$

where $\mathrm{Re}_p = \rho_b |U_p - U_b| d_p / \mu_b$ is particle Reynolds number, according to which the flow regime is determined, and $C^{D,sph}_{b,p}$ and $C^{D,dist}_{b,p}$ are the drag coefficient, respectively, under undistorted particle regime and distorted particle regime.

#### 2.2.2. The drag force between metal and bath

Aluminium and electrolyte tend to separate out for the difference in their densities, and the metal–bath interface was regarded

as a free surface. The drag force between the two liquid phases was calculated with the coefficient $C_{b,m}$ which was given by:

$$C_{b,m} = C^D_{b,m}\rho_{b,m}A_{b,m}|U_b - U_m| \tag{8}$$

Here the drag coefficient between the metal and bath $C^D_{b,m}$ is supposed to be determined by experiments, however, it has not been reported so far that any experiment was carried out to measure the coefficient. Allowing for the intense turbulence at the metal–bath interface in industrial cells and referring to the inertial regime of multiphase flow, the coefficient $C^D_{b,m} = 0.44$ was approximately used. The mixture density $\rho_{b,m}$ and the interfacial density $A_{b,m}$ are defined as, respectively:

$$\rho_{b,m} = r_b\rho_b + r_m\rho_m \tag{9}$$

$$A_{b,m} = \frac{2|\nabla r_b||\nabla r_m|}{|\nabla r_b| + |\nabla r_m|} \tag{10}$$

### 2.3. Calculation of momentum source

The three-dimensional EMFs in the whole fluid region were introduced as a source term in the governing equation. $F_{EM}$ can be calculated from the cross product of electric current density ($J$) and magnetic induction intensity ($B$), as follow:

$$F_{EM} = J \times B \tag{11}$$

The details for obtaining the distribution of electric field and magnetic field by solving corresponding models are given elsewhere (Li et al., 2008).

Another significant external body force affecting the flow is buoyancy aroused by density differences. The buoyancy on the liquid was shown in Table 1, where the density of the bath was fixed as the reference one.

### 2.4. Turbulence model

Inhomogeneous multiphase flow can be solved with fluid-dependent turbulence model. Whereas a more general and computationally less expensive approach is to adopt homogeneous turbulence model, where a single turbulence field is solved instead of two or more separate fields and the mixture density and viscosity are used. Due to its low computational cost and good numerical stability, the homogeneous $k$–$\varepsilon$ turbulence model was applied in this study. The isotropic eddy viscosity ($\mu_T$) is characterized by turbulence kinetic energy ($k$) and its dissipation rate ($\varepsilon$), which are given by:

$$\mu_T = c_\mu\frac{k^2}{\varepsilon} \tag{12}$$

$$\frac{\partial\rho k}{\partial t} + \nabla\cdot(\rho U k) = \nabla\cdot\left[\left(\mu + \frac{\mu_T}{\sigma_k}\right)\nabla k\right] + G_k - \rho\varepsilon \tag{13}$$

$$\frac{\partial\rho\varepsilon}{\partial t} + \nabla\cdot(\rho U\varepsilon) = \nabla\cdot\left[\left(\mu + \frac{\mu_T}{\sigma_\varepsilon}\right)\nabla\varepsilon\right] + \frac{\varepsilon}{k}(C_1G_k - C_2\rho\varepsilon) \tag{14}$$

with

$$\rho = \sum_{\alpha=1}^{3} r_\alpha\rho_\alpha \tag{15}$$

$$\mu = \sum_{\alpha=1}^{3} r_\alpha\mu_\alpha \tag{16}$$

and

$$G_k = \mu_T\nabla U\cdot(\nabla U + \nabla U^T) \tag{17}$$

Here the empirical constants appearing in the model are $c_\mu = 0.09$, $C_1 = 1.44$, $C_2 = 1.92$, $\sigma_k = 1.0$, $\sigma_\varepsilon = 1.3$ (Launder and Spalding, 1972).

### 2.5. Boundary condition

In accordance with the actual situation, anode surfaces were treated as no-slip walls for the liquid, while, inlet boundaries for gas bubbles, and the top face of the bath was regarded as a free-slip wall for the liquid, while, a outlet boundary for gas bubbles, which means a bubble release from the channel when it reaches the surface and then the computation for it is terminated. Other boundaries were taken as no-slip walls for all phases, where wall function (Grotjans and Menter, 1998) was used for the turbulence equations. It is well known the anode gas bubbles mainly consist of $CO_2$ and CO, and the latter is generated by both Boudouard reaction and the reoxidation of reduced entities by $CO_2$, called the back reaction. The gas bubble was treated as a homogeneous phase, and a mass generation rate of the bubbles was defined for the inlet boundaries, despite a small part of $CO_2$ may transform into CO in the bath rather than on anode surfaces. Assuming the mole fraction of $CO_2$ and CO are $a$% and $b$%, respectively, the local mass generation rate of gas bubble $m_{loc}$ (kg s$^{-1}$ m$^{-2}$) was approximately calculated without regard to current efficiency, as follow:

$$m_{loc} \approx \frac{J_a}{10^3F}\frac{22a + 14b}{2a + b} \tag{18}$$

where $J_a$ is local current density on the anode surface (A/m$^2$), and $F$ is Faraday constant.

## 3. Application case and numerical analysis

### 3.1. Case examined

The fluid system of a 300 kA aluminium reduction cell was studied as an application case in this article. The cell, loading the melts, is a rectangular steel shell with the volume of 14.74 m long by 3.74 m wide by 0.44 m high. The metal height is 0.21 m, and the height of the bath, into which 18 × 2 anodes are inserted, is 0.23 m involving 0.05 m interpolar distance. This ACD may be a little large, but it is still in a normal range for many operating cells in China, and a larger ACD is in favor of achieving a steady state for computation. The widths of the interanode channel, the side one, the end one and the center one are 0.04 m, 0.25 m, 0.35 m and 0.10 m, respectively. The main physical parameters used in the computation are shown in Table 2, where the gas bubble consists of 78% $CO_2$ and 22% CO by volume and the parameters of the liquid phases were proposed by Ai (1985). The bubble diameter, obtained by physical modeling, decreases from 18 mm to 7 mm with current density growing from 0.2 A/cm$^2$ to 1.6 A/cm$^2$ (Cassayre et al., 2002). In view of the industrial current density around 0.8A/cm$^2$, the mean diameter of bubbles $d_p$ = 10 mm was approximately adopted in the computation.

The numerical technique for solving the conservation equations was based on the SIMPLEC algorithm. In order to use the finite volume scheme, the computational domain was discretized by an eight nodes hexahedral element. The computational mesh used, shown in Fig. 2, contains 125,744 elements and 141,219 nodes. Nearby the metal–bath interface, dense nodes in vertical direction

**Table 2**
Physical parameters (960 °C).

| | Metal | Bath | Bubble |
|---|---|---|---|
| Density (kg m$^{-3}$) | 2270 | 2130 | 0.398 |
| Dynamic viscosity (kg m$^{-1}$ s$^{-1}$) | $1.18 \times 10^{-3}$ | $2.513 \times 10^{-3}$ | $5.055 \times 10^{-5}$ |

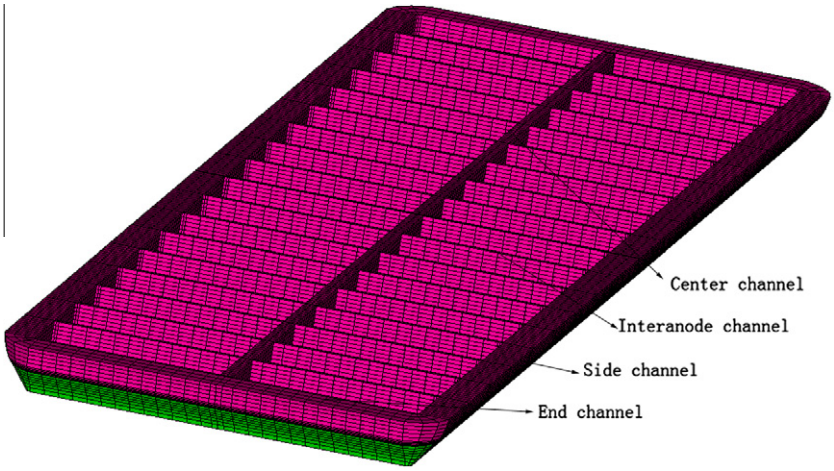


**Fig. 2.** The computational mesh of the 300 kA cell.

were arranged to improve the accuracy of the numerical computation for the free surface. The convergence is indicated by root mean square (RMS) residuals, which are checked for all elements at each time step to ensure the conservation of each variable is attained. The RMS residual of volume fraction must be no more than $10^{-4}$ and those of other variables must be no more than $10^{-5}$ in the computation.

## 4. Results and discussion

To prove the necessity of adopting the three-phase model, two-phase models (bath–bubble model and bath–metal model) of the same cell were also computed, and a comparative study was done by analyzing the calculated results of different models.

Fig. 3 shows the horizontal velocity of electrolyte layer calculated with each model, and the average and maximum velocities are given in Table 3. Contrasting (b) and (c) of Fig. 3, one can see that the bubble phase somewhat disarranges the flow pattern induced by the EMFs, since the bubbles generated on each anode move in separate regions and form a series of small eddies. The behavioral feature of bubbles makes the flow intensity enhanced only in some regions nearby the wall but weakened in the other regions, and consequently the average velocity of the bath decreases to some extent, as shown in Table 3. Comparing (a) with (c) of Fig. 3, it can be seen the influence of the bubble phase on the bath flow is impaired due to the presence of the metal phase that reinforces the flow loops induced by the EMFs, and the result of three-phase model predicts lower velocity. The horizontal velocity vectors on the mid section of the metal layer, shown in Fig. 4, indicates the bubble phase also has certain effect on the metal motion through disturbing the flow loops of the bath, and the bubbles reduces the average velocity of the metal, given in Table 4.

Focusing on the aspect of global flow, the effect of various driven forces, gas bubbles, EMFs, do not complement each other, but show different features independently. The effect of bubbles is greater than that of EMFs in the bath layer, in the metal layer, while, the latter plays a leading role obviously. In the case of the flow under combined effect of bubbles and EMFs, the velocity of the melts is relatively high when any force acts dominantly, nevertheless, the velocity decreases when the intensity of the two forces became closer.

The differences between the predicted metal–bath interface deformation performed by the bath–metal model, shown in Fig. 5, and that performed by the three-phase model, shown in Fig. 6, further confirms each phase is non-negligible. As a result of the bubbles motion, the profiles of anode projection can be observed in Fig. 6, and maximum deviation of the interface from its equilibrium position predicted by the three-phase model is relatively larger.

## 5. An improved model of CE

### 5.1. The mechanism of current loss

The current efficiency normally varies from 87% to 96% in commercial cells (Solli et al., 1997). It is well known that aluminium reacts with cryolite melts at the interface through the formation of reduced entities soluble in the electrolyte, which makes actual production of aluminium lower than theoretical production, defined as current loss. Dissolved sodium (Na(*diss*)) and monovalent aluminium compounds ($AlF_2^-$) are the main reduced products, and the former probably originates from the reaction (Haarberg et al., 1993):

$$Al + 3NaF \rightleftarrows AlF_3 + 3Na(diss) \tag{19}$$

As pointed in relative study (Sterten, 1988), the equilibrium between Na(*diss*) and $AlF_2^-$ is established in the boundary layer at the metal–bath interface by the reaction:

$$NaAlF_2 + NaF \rightleftarrows AlF_3 + 2Na(diss) \tag{20}$$

Since Na(*diss*) appears to have a high diffusion coefficient and transfers through the boundary layer much faster than the other compounds, a rapid transformation of $AlF_2^-$ to Na(*diss*) takes place in the boundary layer, which means Na(*diss*) is probably the most important reduced species concerning the current loss. Thus, the local current loss $i_{loss}$ can be approximately calculated according to:

$$i_{loss} \approx Fk_{Na}(c^*_{Na} - c^{\infty}_{Na}) \tag{21}$$

where $c^*_{Na}$ and $c^{\infty}_{Na}$ are the concentrations of dissolved sodium, respectively, at the metal–bath interface and in the bulk of the bath, and $k_{Na}$ is the mass transfer coefficient of dissolved sodium.

Apparently, in order to calculate the current loss of the cell, the concentrations and the mass transfer coefficient of Na(*diss*) need to be resolved first. Combining theoretical derivation with some empirical equations, Sterten (1988) have presented a method to obtain the concentrations of dissolved sodium and developed a CE model as:

$$i_{loss} = Fk_{Na}c_{Na,eq}\left[-\alpha + \exp\left(-\frac{F}{RT}\eta\right)\right] \tag{22}$$

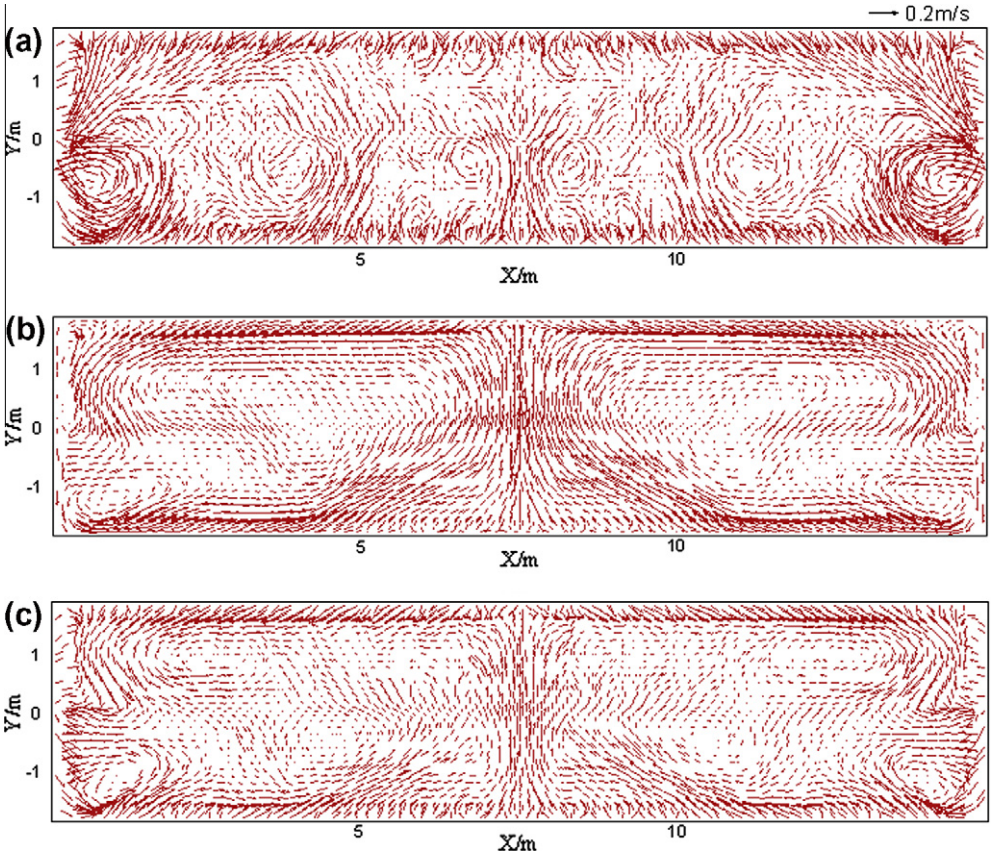


**Fig. 3.** Horizontal velocity vectors of electrolyte layer in the 300 kA cell. (a) The result of bath–bubble model. (b) The result of bath–metal model. (c) The result of three-phase model.

**Table 3**
Maximum and average velocities of bath predicted by different models.

| | $U_{max}$ (m s$^{-1}$) | $U_{avg}$ (m s$^{-1}$) |
|---|---|---|
| Bath–bubble model | 0.2119 | 0.0637 |
| Bath–metal model | 0.1331 | 0.0598 |
| Three-phase model | 0.1572 | 0.0521 |

**Table 4**
Maximum and average velocities of metal predicted by different models.

| | $U_{max}$ (m s$^{-1}$) | $U_{avg}$ (m s$^{-1}$) |
|---|---|---|
| Bath–metal model | 0.2003 | 0.0696 |
| Three-phase model | 0.2173 | 0.0591 |

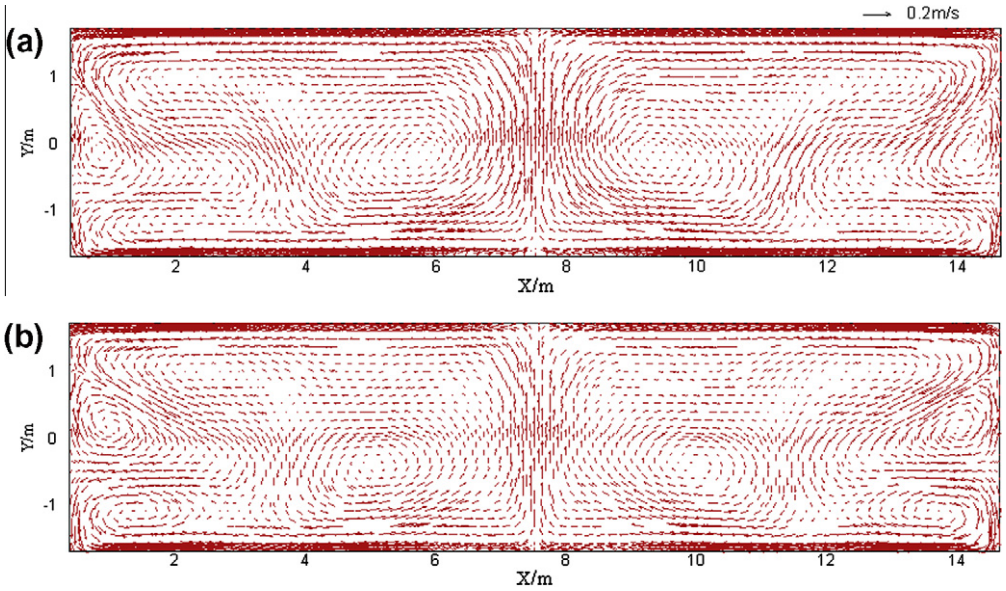


**Fig. 4.** Horizontal velocity vectors of metal melt layer in the 300 kA cell. (a) The result of bath–metal model. (b) The result of three-phase model.

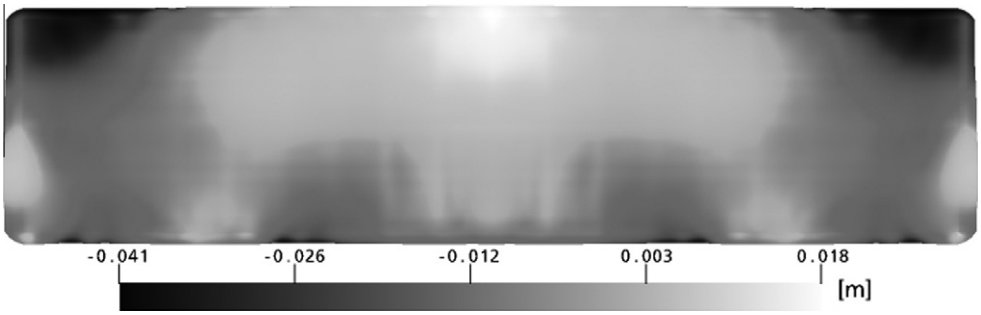


**Fig. 5.** Metal–bath interface deformation obtained by the bath–metal model.

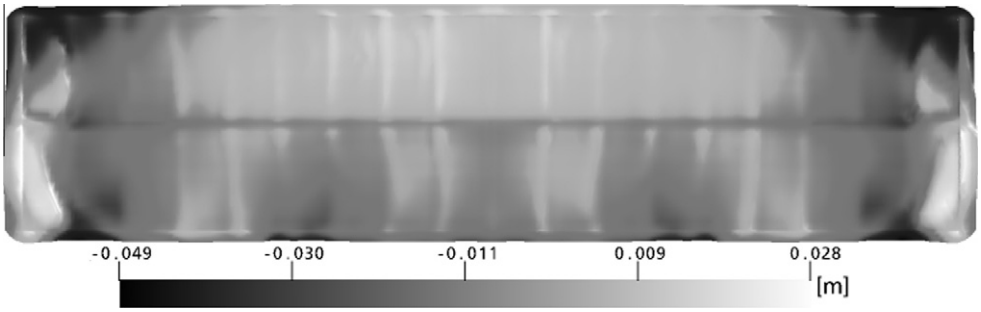


**Fig. 6.** Metal–bath interface deformation obtain by the three-phase model.

where $T$ is temperature, $\eta$ is the concentration overvoltage of aluminium deposition reaction, $c_{Na,eq}$ is the equilibrium concentration of Na(*diss*), a function of temperature and melt composition, in the closed system, and $\alpha$ is the degree of saturation of Na(*diss*) related to the equilibrium value $c_{Na,eq}$ in an open system.

A relationship between $\eta$ (V) and local cathodic current density $i_c$ (A/cm$^2$) is described by the empirical equation, as follow (Solli et al., 1997):

$$\eta = 0.0015R - \frac{0.147Ri_c}{1.97R - 1} \tag{23}$$

where $R$ is molar ratio of electrolyte.

In Sterten's model, the mass transfer coefficient $k_{Na}$ was taken as constant. In commercial cells, however, $k_{Na}$ varies somewhat from one region to another on the metal–bath interface, depending on local melts flow.

### 5.2. Mass transfer coefficient

There are two main classes of theories concerning mass transfer at fluid–fluid interface, which are differentiated by the argument whether the convection can reach the interface (Welty et al., 1984). Haarberg et al. (1998) treated the metal–bath interface as a solid wall, where the convection decreases and falls to zero when the surface is approached, and pointed that the choice is supported by the small ratio between the turbulence energy and the energy of the surface, represented as the metal–bath interfacial tension coefficient of 0.55 Nm$^{-1}$. Based on this, the shear stress on the bottom surface obtained from the two-dimension computation of the bath flow was used to calculate mass transfer coefficient according to a relative model (Davies, 1983). Whereas, the intensely turbulence in cells, at high Reynolds number in magnitude of $10^5$, is capable of bringing bulk fluid to the interface and breaking the stagnant film above the interface, and the numerical predicted turbulence kinetic energy on the interface, in magnitude of $10^{-2}$ J/kg, is high enough to overcome the surface energy, which is also approved by the fact that strong interface perturbation is commonly observed in commercial cells. Consequently, the surface renewal theory in time-average sense is probably more suitable for describing the mass transfer of reduced species at the interface in cells. To calculate the time-average local mass transfer coefficient $k^{L,av}$ the following model was applied (Jajuee et al., 2006):

$$k^{L,av} = \sqrt{\frac{4Ds}{\pi}} \tag{24}$$

where $D$ is diffusion coefficient and $s$ is mean rate of production of fresh surface. Thus, the problem comes down to solve $s$, which can be defined as (Banerjee et al., 1968):

$$s \equiv \frac{v}{l} \tag{25}$$

where $v$ and $l$ are, respectively, the length and velocity scales of eddies. The turbulence was assumed to be isotropic and sufficiently dissipated at the interface, and the following relationships were established according to Kolmogoroffs theory:

$$v = (\upsilon \cdot \varepsilon)^{1/4},\ l = (\upsilon^3/\varepsilon)^{1/4} \tag{26}$$

where $\upsilon = \mu/\rho$ is kinematic viscosity and $\varepsilon$ is turbulence eddy dissipation.

Combination of (25) and (26) provides an expression for $s$, and hence the time-average local mass transfer coefficient becomes:

$$k^{L,av} = \left(\frac{4D}{\pi}\sqrt{\frac{\varepsilon}{\upsilon}}\right)^{\frac{1}{2}} \tag{27}$$

### 5.3. CE calculation

The CE of 300 kA cell was evaluated at the electrolyte composition $R = 2.3$ and the temperature $T = 1233$ k. The kinematic viscosity of bath $\upsilon_b = 1.3 \times 10^{-6}$ m$^2$ s$^{-1}$, the diffusion coefficient of Na(*diss*) $D_{Na} = 1 \times 10^{-8}$ m$^2$ s$^{-1}$ and the degree of saturation of Na(*diss*) $\alpha = 0.5$ (Sterten, 1988) were used in the calculation. The turbulence eddy dissipation on the interface, shown in Fig. 7, was obtained from

the computation of the three-phase flow model, and then the time-average local mass transfer coefficient of Na(*diss*)on the interface was solved referring to the Eq. (27). Combining the computed distribution of current density on the interface, shown in Fig. 8, with the local mass transfer coefficient of Na(*diss*) $k_{Na}^{L,av}$, shown in Fig. 9, the local current loss and CE were calculated successively. Figs. 10 and 11 present the predicted current loss and CE, respectively. One can see that the current loses heavily nearby the tap and duct ends, where

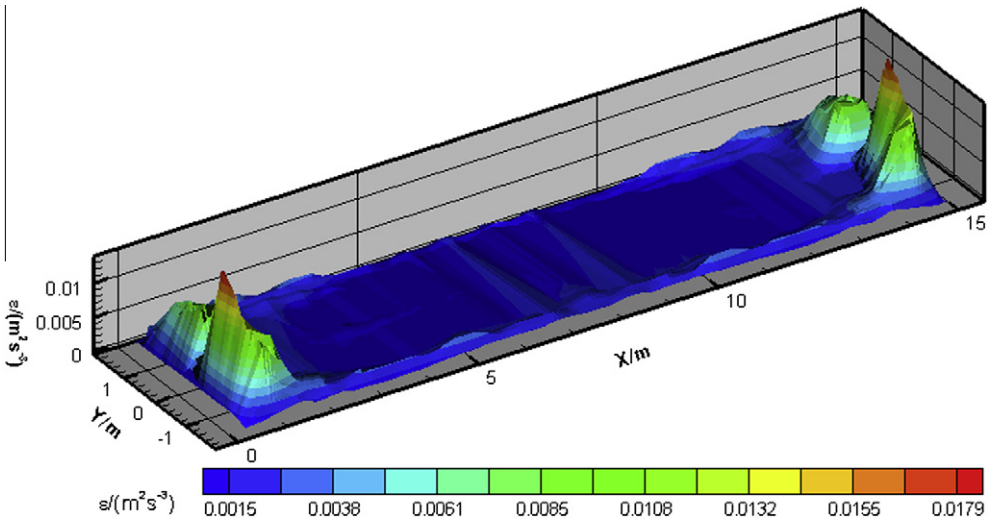


**Fig. 7.** Turbulence eddy dissipation on the interface in 300 kA cell.

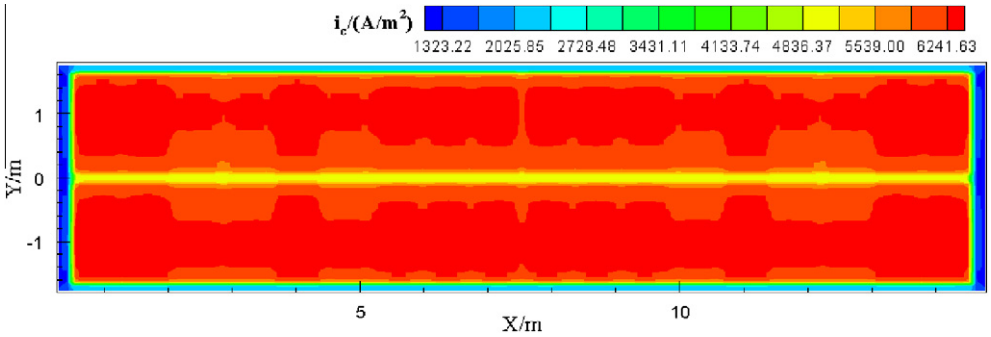


**Fig. 8.** Current density on the metal–bath interface in 300 kA cell.

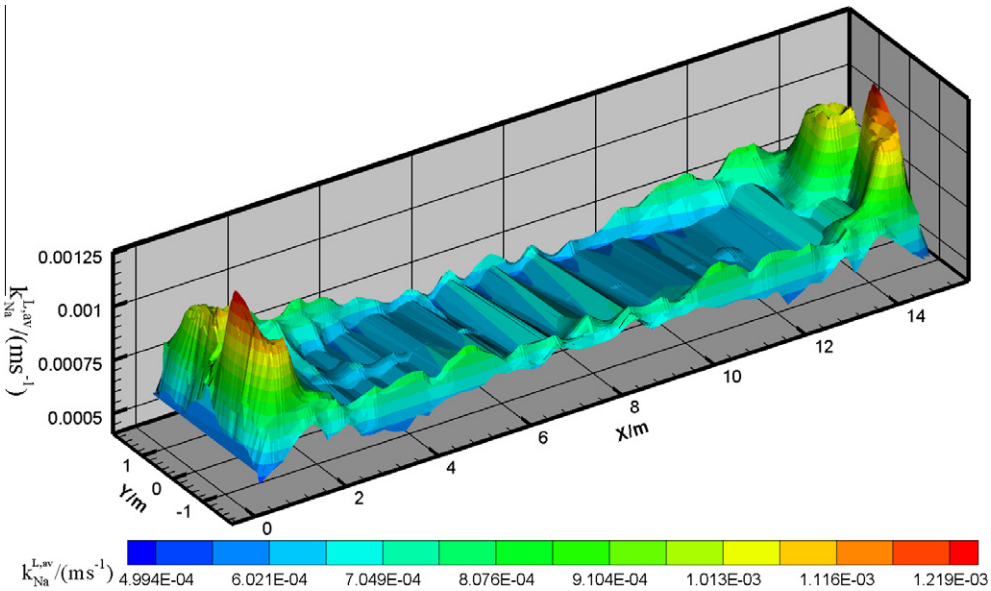


**Fig. 9.** Time-average local mass transfer coefficient of dissolved sodium on the interface in 300 kA cell.

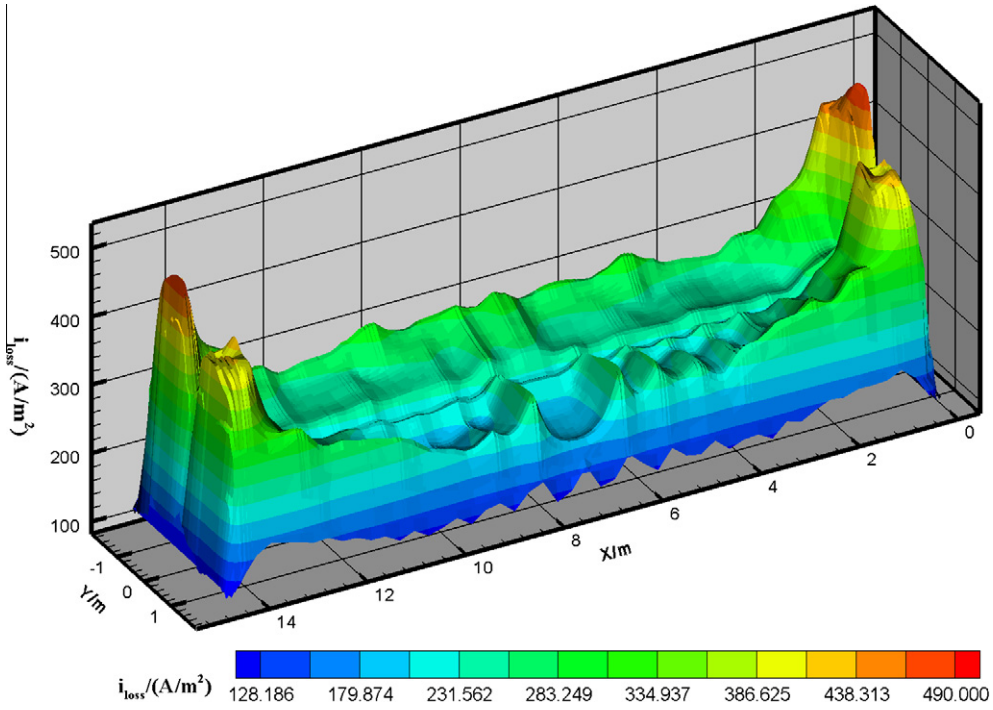


**Fig. 10.** Calculated local current loss in 300 kA cell.

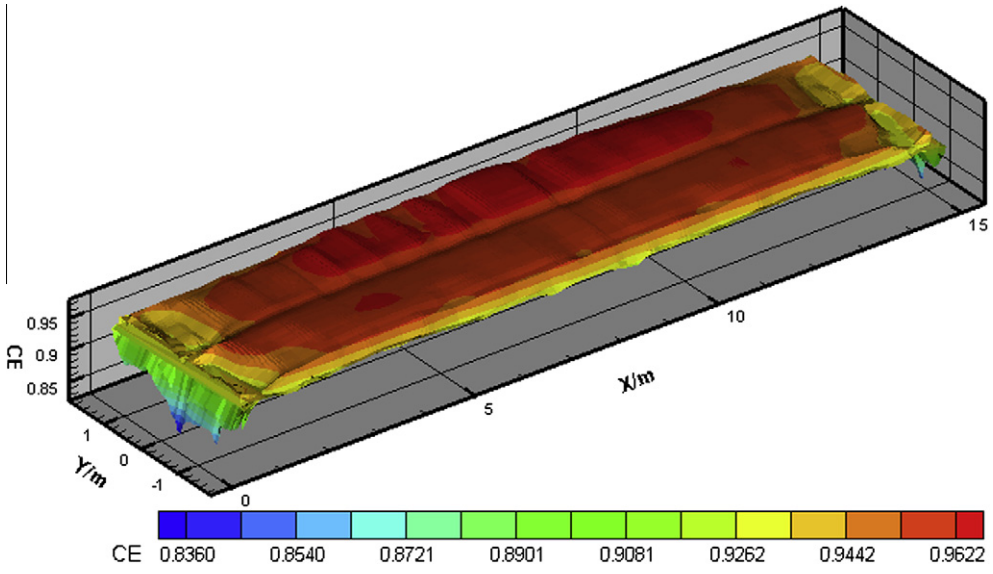


**Fig. 11.** Calculated local current efficiency in 300 kA cell.

the turbulence dissipates rapidly, as shown in Fig. 7. The low local current density results in the small current loss in center and side channels, where the comparative low CE presents, which indicates that increasing local current density is in favor of improving CE. As a result of both the low current density and high mass transfer coefficient, the CE nearby the two ends is excessive low.

Overall, the CE distribution feature is that the regions beneath the anodes present a comparative high CE and CE in the half of the cell closed to the downstream side is higher than that in the other half. The maximum and minimum local CEs are 97.1% and 82.7%. The predicted CE of the whole cell is 95.0%, which is a reasonable value but may be a little higher than the actual CE due to some extra small parts of current loss not covered in the model. The further validation for the predicted local CE is hindered by the huge difficulty in industrial measurement.

## 6. Conclusions

An inhomogeneous three-phase model was established to solve the melts (bath and metal) flow in aluminium reduction cells. As an application case, the flow in a 300 kA cell was numerically computed with the model by using the finite volume scheme, and the results show that both the flow field of the melts and the metal–bath interface deformation predicted by the three-phase model present some important characteristics, which the two-phase models fail to predict. The globality of the flow in cells is approved

to be non-negligible. The improved model of CE relates turbulence eddy dissipation on the metal–bath interface with local current loss, based on the surface renewal theory, which is more befitting for describing the mass transfer of reduced entities in cells. With the model the distribution of CE in the 300 kA cell was predicted, and the calculated CE value of the whole cell is reasonable. The models presented in this paper can be used in the design and optimization of large-scale aluminium reduction cells, so as to realize the target of raising current efficiency and saving energy.

## Acknowledgements

The authors are grateful for the financial support of the National Basic Research Program of China (2005CB623703) and the National High-Tech Research and Development Program of China (2008AA030504).

## References

Ai, D.K., 1985. Hydrodynamics of the Hall–Héroult cell. Light Metals 593, 607.
Banerjee, S., Scott, D., Rhodes, E., 1968. Mass transfer to falling wavy liquid films in turbulent flow. Ind. Eng. Chem. Fundam. 7 (1), 22–27.
Blanc, J.M., Entner, P., 1980. Application of computer calculations to improve electromagnetic behaviour of pots. Light Metals 285, 295.
Cassayre, L., Utigard, T.A., Bouvet, S., 2002. Visualizing gas evolution on graphite and oxygen-evolving anodes. JOM 54 (5), 41–45.
Davies, J.T., 1983. A new theory of aerosol deposition from turbulent fluids. Chem. Eng. Sci. 38, 135–139.
Doheim, M.A., El-Kersh, A.M., Ali, M.M., 2007. Computational modeling of flow in aluminum reduction cells due to gas bubbles and electromagnetic forces. Metall. Mater. Trans. B 38 (1), 113–119.
Grotjans, H., Menter, F.R., 1998. Wall functions for general application CFD codes. In: Proceedings of the 4th Computational Fluid Dynamics conference, vol. 1, pp. 1112–1117.
Haarberg, G.M., Osen, K.S., Thonstad, J., et al., 1993. Measurement of electronic conduction in cryolite alumina melts and estimation of its effect on current efficiency. Metall. Trans. B 24b, 729–735.
Haarberg, T., Solheim, A., Johansen, S., et al., 1998. Effect of anodic gas release on current efficiency in Hall–Heroult cells. Light Metals 475, 481.
Ishii, M., Zuber, N., 1979. Drag coefficient and relative velocity in bubbly, droplet or particulate flows. AIChE J. 25, 843–855.
Jajuee, B., Margaritis, A., Karamanev, D., Bergougnou, M., 2006. Application of surface-renewal-stretch model for interface mass transfer. Chem. Eng. Sci. 61, 3917–3929.
Launder, B.E., Spalding, D.B., 1972. Mathematical Models of Turbulence. Academic Press, London.
Li, J., Liu, W., Lai, Y.Q., et al., 2008. An improved finite-element model for electromagnetic analysis in aluminum cells. JOM 60 (2), 58–61.
Robl, R.F., 1983. Metal flow dependence on ledging in Hall–Héroult cells. Light Metals 449, 456.
Severo, D.S., Schneider, A.F., Pinto, E.C.V., et al., 2005. Modeling magnetohydrodynamics of aluminum electrolysis cells with ANSYS and CFX. Light Metals 475, 480.
Solli, P.A., Eggen, T., Skybakmoen, E., Sterten, A., 1997. Current efficiency in the Hall–Heroult process for aluminium electrolysis: experimental and modelling studies. J. Appl. Electrochem. 27, 939–946.
Sterten, A., 1988. Current efficiency in aluminium reduction cells. J. Appl. Electrochem. 18, 473–483.
Welty, J.R., Wicks, C.E., Wilson, R.E., 1984. Fundamentals of Momentum, Heat, and Mass Transfer. John Wiley & Sons, New York.
Wu, J., Huang, M., Huang, J., et al., 2003. Computation of flow field of electrolyte-aluminium liquid and surface distortion of aluminum liquid in reduction cell. Trans. Nonferrous Met. Soc. China 13 (1), 241–244 (In Chinese).
Zhou, P., Zhou, N.J., Mei, C., et al., 2003. Numerical calculation and industrial measurements of metal pad velocities in Hall–Héroult cells. Trans. Nonferrous Met. Soc. China 13 (1), 208–212.